mathematics

MDPI

Article

A Modified Radial Point Interpolation Method (M-RPIM) for Free Vibration Analysis of Two-Dimensional Solids

Tingting Sun [1,2], Peng Wang [3], Guanjun Zhang [2] and Yingbin Chai [2,4,*]

[1] School of Road Bridge & Harbor Engineering, Nanjing Vocational Institute of Transport Technology, Nanjing 211188, China
[2] School of Naval Architecture, Ocean and Energy Power Engineering, Wuhan University of Technology, Wuhan 430063, China
[3] Wuhan Second Ship Design and Research Institute, Wuhan 430205, China
[4] State Key Laboratory of Ocean Engineering, Shanghai Jiao Tong University, Shanghai 200240, China
* Correspondence: chaiyb@whut.edu.cn

Abstract: The classical radial point interpolation method (RPIM) is a powerful meshfree numerical technique for engineering computation. In the original RPIM, the moving support domain for the quadrature point is usually employed for the field function approximation, but the local supports of the nodal shape functions are always not in alignment with the integration cells constructed for numerical integration. This misalignment can result in additional numerical integration error and lead to a loss in computation accuracy. In this work, a modified RPIM (M-RPIM) is proposed to address this issue. In the present M-RPIM, the misalignment between the constructed integration cells and the nodal shape function supports is successfully overcome by using a fixed support domain that can be easily constructed by the geometrical center of the integration cell. Several numerical examples of free vibration analysis are conducted to evaluate the abilities of the present M-RPIM and it is found that the computation accuracy of the original RPIM can be markedly improved by the present M-RPIM.

Keywords: meshfree numerical technique; free vibration; integration error; numerical integration

MSC: 35A08; 35A09; 35A24; 65L60; 74S05

Citation: Sun, T.; Wang, P.; Zhang, G.; Chai, Y. A Modified Radial Point Interpolation Method (M-RPIM) for Free Vibration Analysis of Two-Dimensional Solids. *Mathematics* **2022**, *10*, 2889. https://doi.org/10.3390/math10162889

Academic Editor: André Nicolet

Received: 21 July 2022
Accepted: 9 August 2022
Published: 12 August 2022

1. Introduction

The classical finite element method (FEM), which is based on the weighted residual technique, is a versatile and well-developed numerical approach in the field of modern computation mechanics [1]. Many mature commercial software packages (such as ANSYS, ABAQUS and NASTRAN) based on the FE approach have been developed and used in various engineering applications. Though the standard FEM has achieved great success in practical engineering computation, the FEM still suffers from several inherent shortcomings compared to other advanced numerical techniques [2–12]. Among them, one important issue is that the FEM is essentially a mesh-based method and the involved problem domain should be firstly discretized into a series of elements that are connected by nodes for FE analysis. Therefore, the additional burdensome tasks for meshing operations cannot always be circumvented. Additionally, the solution accuracy of the FEM is usually sensitive to mesh qualities and the solutions from low-quality meshes are always not sufficiently accurate. To obtain sufficiently fine solutions, more attention should be given to obtain high-quality meshes. These issues will be greater when the standard FEM is employed to manage problems related to dynamic cracks and large deformation of complicated geometric shapes.

To alleviate the dependence of the conventional FE approach on predefined meshes, a series of smoothed FEMs [13–17] and meshfree techniques [18–24] have been proposed,

such as the element-free Galerkin method (EFGM) [25,26], the meshless local Petrov–Galerkin method (MLPG) [27], the reproducing kernel particle method (RKPM) [28], the radial point interpolation method (RPIM) [29,30], the general finite difference method GFDM [31–35], and the boundary-based numerical methods [36–40], to name a few. Actually, the meshfree methods can be classified into different types according to different formulation procedures [18]. Among them, several meshless methods are based on the weak form of the governing equation [41–44], while some others are based on the strong weak form [45–51]. In this work, we mainly focus on discussing the meshfree methods based on the well-known Galerkin weighted residual technique (such as the EFEM and RPIM), which are the typical weak-form-based numerical techniques. Compared to the standard FEM, one outstanding advantage of these meshfree methods is that the required nodal shape functions can be built entirely by using a set of scattered nodes, rather than as elements in the conventional FEM. In consequence, the field function approximation also can be constructed by the scattered nodes. This property enables the meshfree methods to have distinct advantages over the conventional FEM in managing the dynamic crack problem and larger deformation problem. In addition, adaptive analysis also can be implemented much more easily in the meshfree framework than in the standard FEM framework. More importantly, the meshfree methods usually possess other excellent features that the standard FEM does not have. A very good comparison and overview on the meshfree methods and the FEM can be found in a published monograph [18].

Although the meshfree methods have achieved considerable success both in theory and practical engineering applications, they still cannot match the classical FEM in terms of universality; further, there still exists several crucial issues that should be addressed very carefully. For example, the radial point interpolation method (RPIM), which is a typical meshfree numerical method, has been employed for solving many engineering problems owing to several excellent features, such as relatively high computation accuracy, good numerical stability and the possession of the Kronecker-delta function property. However, the compatibility of the standard RPIM cannot be automatically ensured, which may lead to numerical integration error. The main reason is that in the standard RPIM the local support domains of nodal interpolation functions are not always in accord with the constructed integration cells for numerical integration. The related issues have been investigated in [52,53] and in the so-called bounding box technique that has been proposed by proposed by Dolbow and Belytschko [52]. The related numerical results show that this scheme is indeed quite effective in addressing the issues mentioned; however, the implementation of this scheme is quite complicated and, hence, it is not very practical in engineering computation.

In this work, a simple and elegant scheme is developed to make the local support domains of the nodal shape functions in RPIM entirely align with the constructed quadrature cells for numerical integration; hence, the possible integration error can be markedly decreased. The main idea of this scheme is to design a new node selection scheme for the field function approximation. In this scheme, a fixed support domain (not a moving support domain in the original RPIM), which is determined by the geometrical center of the quadrature cell, is used for any quadrature point in the integration cell. For the convenience of notation, the proposed scheme in this work is called the modified RPIM (M-RPIM). We have further employed the present M-RPIM to analyze the free vibration of two-dimensional solids. It can be found that the M-RPIM behaves much better than the original RPIM for free vibration analysis, and many more numerical solutions can be provided with the totally identical node distributions.

2. Formulation of the Original RPIM and the Present M-RPIM

Consider a problem domain Ω with boundary Γ, and a field function $u(\mathbf{x})$ is defined on it. A series of scattered field nodes are employed to totally discretize the problem domain and its boundary. For a sampling point in the problem domain, the corresponding field

function approximation $u_h(\mathbf{x})$ can be expressed in the following form by using the radial basis function (RBF) and polynomial basis function (PBF) [18]:

$$u_h(\mathbf{x}) = \sum_{i=1}^{n} R_i(\mathbf{x})a_i + \sum_{j=1}^{m} P_j(\mathbf{x})b_j = \mathbf{R}^T(\mathbf{x})\mathbf{a} + \mathbf{P}^T(\mathbf{x})\mathbf{b}, \tag{1}$$

in which $R_i(\mathbf{x})$ stands for the RBF used and $P_j(\mathbf{x})$ represents the PBF used; n denotes the number of RBF used for interpolation, namely, there are n field nodes in the support domain of the sampling point $\mathbf{x}$, m denotes the number of PBF used for interpolation, and the complete linear polynomial ($[1\ x\ y]$) is used in this work, namely, $m = 3$; a_i and b_j are the unknown interpolation coefficients.

There are many different types of RBF that can be used to formulate the RPIM, and different RBFs have different features [18]. In this work, the well-known multiquadrics (MQ) function is used to construct the required field function approximation owing to its several excellent characteristics. The expression of the MQ function is as follows [18,21]:

$$R_i(\mathbf{x}) = \left[r_i^2 + (\alpha_c d_c)^2\right]^q, \tag{2}$$

in which r_i denotes the distance from the field node to the sampling point, d_c is the average nodal interval of the field nodes used, and α_c and q denote two undetermined parameters that are closely related to the computation accuracy of the RPIM; $q = 1.03$ and $\alpha_c = 1$ are used in this work because very good numerical results can always be obtained for solid mechanics with these parameters.

With the aim to determine the coefficients a_i and b_j, Equation (1) should satisfy a series of reasonable constraint conditions. Firstly, it is usually assumed that the constructed field function approximation can exactly pass through the function values of all the nodes located in the support domain of the sampling point $\mathbf{x}$; these constraints can be expressed by:

$$\begin{bmatrix} u_1 & u_2 & \cdots & u_n \end{bmatrix}^T = \mathbf{R}_0\mathbf{a} + \mathbf{P}_0\mathbf{b}, \tag{3}$$

$$\mathbf{R}_0 = \begin{bmatrix} R_1(r_1) & R_2(r_1) & \cdots & R_n(r_1) \\ R_1(r_2) & R_2(r_2) & \cdots & R_n(r_2) \\ \vdots & \vdots & \vdots & \vdots \\ R_1(r_n) & R_2(r_n) & \cdots & R_n(r_n) \end{bmatrix}, \tag{4}$$

$$\mathbf{P}_0^T = \begin{bmatrix} 1 & 1 & \cdots & 1 \\ x_1 & x_2 & \cdots & x_n \\ y_1 & y_2 & \cdots & y_n \\ \vdots & \vdots & \ddots & \vdots \\ q_m(\mathbf{x}_1) & q_m(\mathbf{x}_2) & \cdots & q_m(\mathbf{x}_n) \end{bmatrix}, \tag{5}$$

in which $\mathbf{R}_0$ and $\mathbf{P}_0$ are the so-called moment matrices corresponding to the RBF and PBF, respectively.

To uniquely determine the unknown interpolation coefficients a_i and b_j, the following additional constraints should also be satisfied:

$$\sum_{i=1}^{n} P_j(\mathbf{x}_i)a_i = \mathbf{P}_0^T\mathbf{a} = 0, j = 1, 2, \cdots, m, \tag{6}$$

The combination of all the constraining conditions shown in Equations (2) and (6) can result in the following matrix equation:

$$\begin{bmatrix} \mathbf{u} \\ 0 \end{bmatrix} = \underbrace{\begin{bmatrix} \mathbf{R}_0 & \mathbf{P}_0 \\ \mathbf{P}_0^T & 0 \end{bmatrix}}_{\mathbf{G}} \underbrace{\begin{bmatrix} \mathbf{a} \\ \mathbf{b} \end{bmatrix}}_{\mathbf{a}_0} = \mathbf{G}\mathbf{a}_0, \tag{7}$$

Then, the undetermined interpolation coefficients can be calculated by

$$\begin{bmatrix} \mathbf{a} \\ \mathbf{b} \end{bmatrix} = \mathbf{a}_0 = \mathbf{G}^{-1} \begin{bmatrix} \mathbf{u} \\ 0 \end{bmatrix}, \tag{8}$$

Substituting the interpolation coefficients obtained into Equation (1) and following the standard formulation of the conventional RPIM, the required nodal interpolation shape function can be obtained by

$$\Phi^T(\mathbf{x}) = \begin{bmatrix} \phi_1(\mathbf{x}) & \phi_2(\mathbf{x}) & \cdots & \phi_n(\mathbf{x}) \end{bmatrix} = \begin{Bmatrix} \mathbf{R}^T(\mathbf{x}) & \mathbf{Q}^T(\mathbf{x}) \end{Bmatrix} \mathbf{G}^{-1}|_{1\sim n}, \tag{9}$$

In the standard RPIM, the field nodes participating in building the field function approximation for the sampling point, which are usually quadrature points, are determined by a support domain. The shape of the support domain can be a square or a circle. The sampling point is usually the center of the defined support domain, while the background cells for numerical integration are always constructed independently of the support domain. As a result, the different sampling points (or quadrature points) in one integration cell may have different support domains, namely, the required field nodes to construct the field function approximation are different. In summary, since the moving support domain is used in the traditional RPIM, the support domain of the nodal shape functions always do not align with the background integration cells, which then leads to considerable numerical integration error and degrades the quality of the numerical solutions obtained.

To effectively overcome the abovementioned misalignment between the nodal shape function supports and the background integration cells, in this work a modified RPIM (M-RPIM) is employed to analyze the free vibration of two-dimensional solids. In this M-RPIM, a fixed support domain (as shown in Figure 1) rather than the moving support domain in the standard RPIM is used to select the required field nodes for the construction of the field function approximation. In other words, the identical field nodes are used for interpolation for any quadrature points in one background integration cell. The fixed support domain used can still be a square or a circle (the square support domain is used in this work); however, this fixed support domain is always centered by the geometrical center of the integration cell, not centered by the sampling points (which are usually the quadrature points) as in the conventional RPIM. The difference between the original RPIM and the present M-RPIM in constructing the field function approximation can be shown as follows:

$$\begin{cases} u_h(\mathbf{x})_{\mathrm{RPIM}} = \sum \phi_i u_i, x_i \in \Omega^Q \\ u_h(\mathbf{x})_{\mathrm{M-RPIM}} = \sum \phi_i u_i, x_i \in \Omega^* \end{cases}, \tag{10}$$

in which Ω^Q stands for the moving support domains, which are centered by the quadrature points in one background cell, Ω^* represents the fixed support domains that are directly centered by the centroids of the background integration cells.

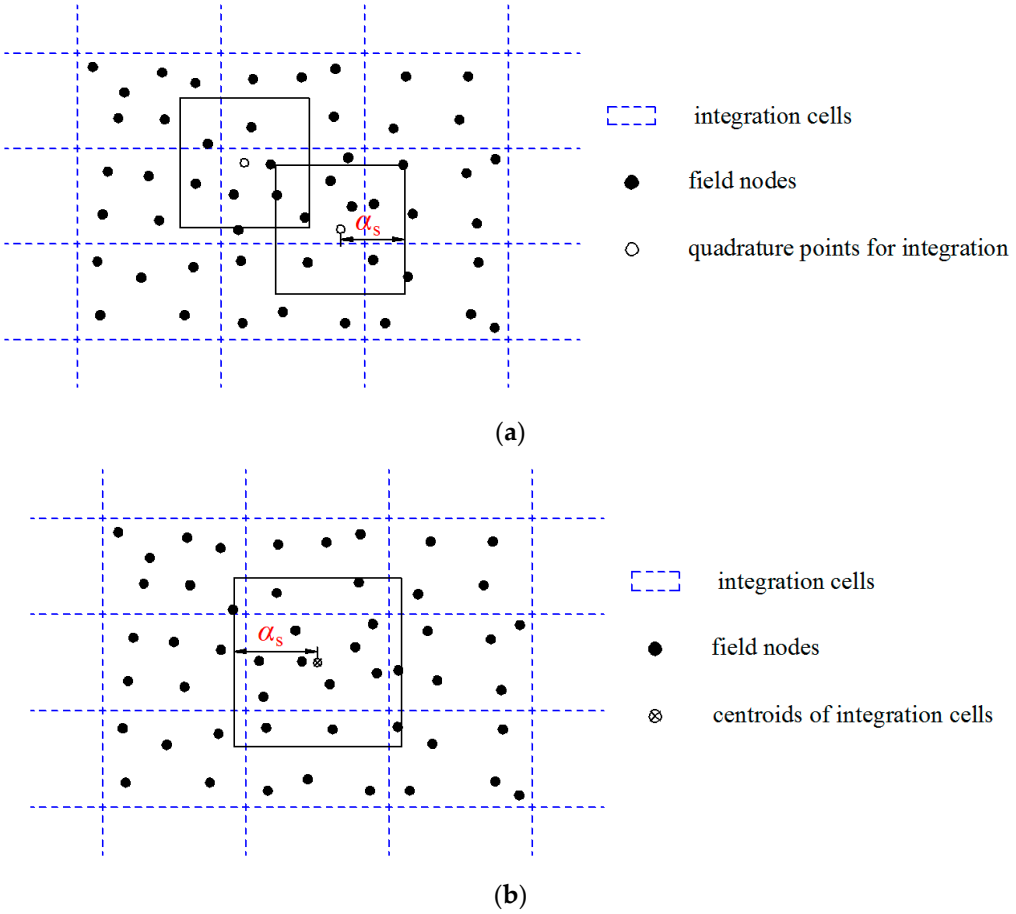

Figure 1. Comparison of the original RPIM and the present M-RPIM for node selection in the numerical approximation. (**a**) The node selection scheme in the original RPIM. (**b**) The node selection scheme in the present M-RPIM.

3. Formulation of the Elastodynamics of Two-Dimensional Solids

Based on the small displacement assumption, the partial differential equation (PDE) of the boundary-value problem for the elastodynamics of solids can be written by

$$\nabla \boldsymbol{\sigma} + \mathbf{b} = \rho \ddot{\mathbf{u}} \text{ in } \Omega, \tag{11}$$

in which Ω denotes the problem domain considered, $\mathbf{b}$ stands for the body force, $\boldsymbol{\sigma}$ represents the stress tensor, ρ is the mass density, $\mathbf{u}$ is the displacement vector and $\ddot{\mathbf{u}}$ signifies second derivatives of $\mathbf{u}$.

As usual, the following two kinds of boundary conditions are always considered for the two-dimensional elastodynamics of solids:

$$\begin{cases} \mathbf{u} = \bar{\mathbf{u}}, & \text{on } \Gamma_E \\ \boldsymbol{\sigma} \cdot \mathbf{n} = \bar{\mathbf{t}}, & \text{on } \Gamma_N \end{cases}, \tag{12}$$

in which Γ_E and Γ_N denote the essential boundary condition and the natural boundary condition, respectively; $\bar{\mathbf{u}}$ and $\bar{\mathbf{t}}$ are the imposed displacement vector and traction vector on the corresponding boundary conditions.

Using the boundary conditions shown in Equation (12) and following the virtual displacement principle, the weak form of Equation (11) for the elastodynamics of two-dimensional solids can be obtained by

$$\int_{\Omega} \rho \delta \mathbf{u} \ddot{\mathbf{u}} \mathrm{d}\Omega + \int_{\Omega} \delta \boldsymbol{\varepsilon} \boldsymbol{\sigma} \mathrm{d} = \int_{\Gamma_N} \delta \mathbf{u} \, \bar{\mathbf{t}} \, \mathrm{d}\Gamma + \int_{\Omega} \delta \mathbf{u} \mathbf{b} \mathrm{d}\Omega, \tag{13}$$

in which $\delta \mathbf{u}$ and $\delta \boldsymbol{\varepsilon}$ stand for the virtual displacement and strain, respectively.

Using the Galerkin weighted residual techniques and the field function approximation shown in Equation (1), the matrix equation for the weak form shown in Equation (13) can be obtained [1,18] by the following relationship:

$$\mathbf{M}\ddot{\mathbf{u}} + \mathbf{C}\dot{\mathbf{u}} + \mathbf{K}\mathbf{u} = \mathbf{F}, \tag{14}$$

in which $\mathbf{M}$ is the usual mass matrix, $\mathbf{K}$ is the usual stiffness matrix, $\mathbf{F}$ is the applied force vector and $\mathbf{C}$ is the matrix containing the damping effects.

Without considering the damping effects and the external force, Equation (14) reduces to

$$\mathbf{M}\ddot{\mathbf{u}} + \mathbf{K}\mathbf{u} = 0, \tag{15}$$

Equation (15) is the governing matrix equation obtained for the free vibration analysis of two-dimensional solids.

Assuming that the displacement solution to Equation (15) is time harmonic, namely,

$$\mathbf{u} = \mathbf{U} \exp(j\omega t), \tag{16}$$

in which $j = \sqrt{-1}$, ω denotes the angular frequency, and $\mathbf{U}$ is the amplitude of the displacement distribution.

Substituting Equation (16) into Equation (15), then Equation (15) can be rewritten as

$$\left[\mathbf{K} - \omega^2 \mathbf{M}\right] \mathbf{U} = 0, \tag{17}$$

From Equation (17), we can observe that the typical eigenvalue problem should be solved to perform the analysis of free vibration problems.

4. Numerical Example

In this section, several typical numerical examples are considered to assess the capability of the proposed M-RPIM in free vibration analysis of the two-dimensional solids. For the convenience of discussion, the natural frequency values from the present M-RPIM are compared to those from the original RPIM and the standard finite element approach with bilinear quadrilateral elements (FEM-Q4). In all the numerical examples considered, identical node arrangements are employed for these three different numerical methods (M-RPIM, RPIM and FEM-Q4). For simplification, the quadrilateral meshes used are directly employed as the background cells to perform the numerical integration for the RPIM and M-RPIM, unless otherwise noted. To effectively examine and compare the accuracy and convergence of numerical solutions from the different numerical methods, the following relative error indicator is employed in this work:

$$\mathrm{Re} = \left| \frac{f_{num} - f_{ref}}{f_{ref}} \right| \times 100\%, \tag{18}$$

in which f_{num} denotes the natural frequency results from the numerical methods (M-RPIM, RPIM and FEM-Q4) and f_{ref} represents the reference natural frequency results, which are usually obtained from the commercial finite element software packages with a very refined mesh.

4.1. Free Vibration Analysis of the Cantilever Beam

Firstly, the free vibration of a cantilever beam is considered here. As shown in Figure 2, the geometric configuration of the cantilever beam has length L = 100 mm and height D = 10 mm. A unit thickness (t = 1 mm) is considered for this beam and, hence, this numerical example can be simplified as a plane stress problem. The material constants of this beam are taken as Young's modulus $E = 2.1 \times 10^{11}$ Pa, Poisson's ratio v = 0.3 and mass density $\rho = 8 \times 10^3$ kg/m^3. The regular node arrangements are used to discretize the problem domain of this cantilever beam for the three different numerical methods. For a detailed analysis and discussion, a series of different node arrangement patterns with different nodal intervals are used here (see Figure 3).

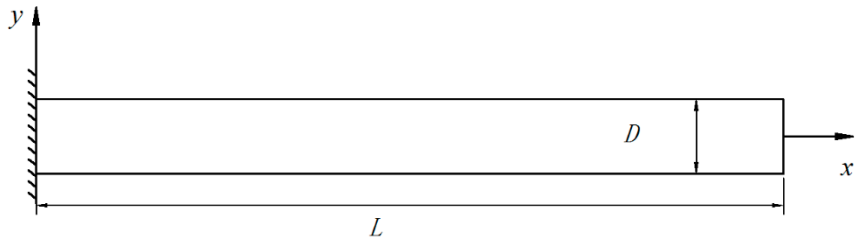

Figure 2. The geometric configuration of the cantilever beam in plane stress condition.

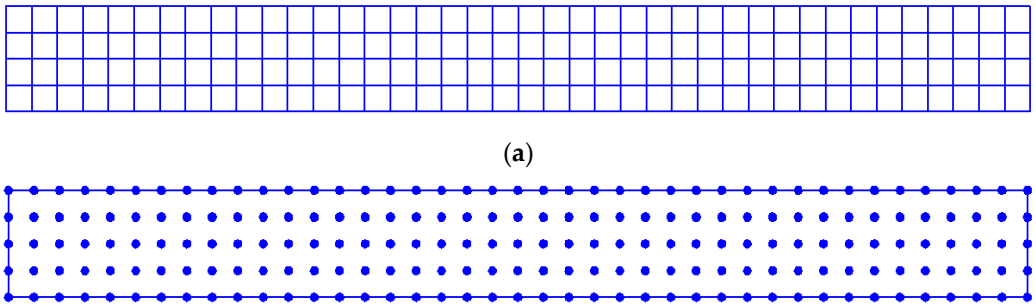

(**a**)

(**b**)

Figure 3. The different node arrangement patterns that are employed to discretize the cantilever beam for different numerical methods: (**a**) uniform mesh pattern, which is used to discretize the cantilever beam for the standard FEM-Q4; (**b**) node arrangement pattern used to discretize the cantilever beam for the RPIM and M-RPIM.

4.1.1. Computation Accuracy Study

Utilizing a series of different node arrangement patterns, the first twelve natural frequency solutions from the three numerical methods are listed in Tables 1–4. Among them, the corresponding RPIM and M-RPIM solutions are obtained when the size of the nodal support domain is taken as $\alpha_s = 2.5h$ (h denotes average nodal interval of the meshes used). The reference solutions from eight-node quadrilateral element (FEM-Q8) with a very refined mesh pattern (average nodal interval h = 0.1 mm) are also provided in the tables for comparison.

Table 1. The first twelve natural frequency solutions from the three numerical methods using the node arrangement pattern with average nodal space h = 2 mm.

Mode	FEM-Q4	Error (%)	RPIM	Error (%)	M-RPIM	Error (%)	Ref.
1	830.567	1.003	815.423	0.839	825.213	0.351	822.322
2	4989.034	1.132	4909.931	0.471	4952.383	0.389	4933.177
3	12,826.933	0.022	12,826.322	0.017	12,825.428	0.010	12,824.145
4	13,167.852	1.336	13,035.277	0.316	13,025.003	0.237	12,994.215
5	23,992.489	1.604	23,772.722	0.673	23,725.015	0.471	23,613.775
6	36,701.000	1.910	36,492.012	1.329	36,197.042	0.510	36,013.226
7	38,467.305	0.059	38,461.345	0.044	38,450.819	0.016	38,444.488
8	50,697.394	2.248	50,570.105	1.991	49,854.144	0.547	49,582.799
9	64,062.116	0.225	64,045.638	0.199	63,984.254	0.103	63,918.563
10	65,590.504	2.524	65,609.724	2.554	64,290.994	0.493	63,975.503
11	81,118.869	3.012	81,334.286	3.286	79,233.413	0.618	78,746.943
12	89,562.090	0.252	89,514.438	0.199	89,345.277	0.010	89,336.686

Table 2. The first twelve natural frequency solutions from the three numerical methods using the node arrangement pattern with average nodal space h = 1 mm.

Mode	FEM-Q4	Error (%)	RPIM	Error (%)	M-RPIM	Error (%)	Ref.
1	824.304	0.241	819.913	0.293	822.800	0.058	822.322
2	4946.701	0.274	4924.719	0.171	4936.588	0.069	4933.177
3	12,824.618	0.004	12,824.955	0.006	12,824.496	0.003	12,824.145
4	13,036.557	0.326	13,008.259	0.108	13,004.647	0.080	12,994.215
5	23,706.655	0.393	23,657.845	0.187	23,635.380	0.091	23,613.775
6	36,182.573	0.470	36,152.539	0.387	36,049.829	0.102	36,013.226
7	38,449.523	0.013	38,447.183	0.007	38,445.401	0.002	38,444.488
8	49,857.999	0.555	49,874.211	0.588	49,637.697	0.111	49,582.799
9	63,996.004	0.121	63,990.287	0.112	63,976.475	0.091	63,918.563
10	64,332.241	0.558	64,422.173	0.698	63,994.651	0.030	63,975.503
11	79,334.621	0.746	79,524.455	0.987	78,846.611	0.127	78,746.943
12	89,391.481	0.061	89,377.038	0.045	89,336.977	0.000	89,336.686

Table 3. The first twelve natural frequency solutions from the three numerical methods using the node arrangement pattern with average nodal space h = 0.67 mm.

Mode	FEM-Q4	Error (%)	RPIM	Error (%)	M-RPIM	Error (%)	Ref.
1	823.104	0.095	821.051	0.155	822.413	0.011	822.322
2	4938.559	0.109	4928.453	0.096	4933.920	0.015	4933.177
3	12,824.010	0.001	12,823.612	0.004	12,823.953	0.001	12,824.145
4	13,011.299	0.131	12,992.024	0.017	12,996.698	0.019	12,994.215
5	23,651.752	0.161	23,631.689	0.076	23,619.234	0.023	23,613.775
6	36,083.214	0.194	36,074.813	0.171	36,022.821	0.027	36,013.226
7	38,445.687	0.003	38,444.328	0.000	38,443.843	0.002	38,444.488
8	49,697.499	0.231	49,714.721	0.266	49,597.527	0.030	49,582.799
9	63,982.840	0.101	63,979.749	0.096	63,939.314	0.032	63,918.563
10	64,092.160	0.182	64,149.033	0.271	63,974.133	0.002	63,975.503
11	78,994.780	0.315	79,104.908	0.455	78,774.275	0.035	78,746.943
12	89,358.561	0.024	89,351.356	0.016	89,334.272	0.003	89,336.686

Table 4. The first twelve natural frequency solutions from the three numerical methods using the node arrangement pattern with average nodal space h = 0.5 mm.

Mode	FEM-Q4	Error (%)	RPIM	Error (%)	M-RPIM	Error (%)	Ref.
1	822.674	0.043	821.486	0.102	822.279	0.005	822.322
2	4935.637	0.050	4929.842	0.068	4932.985	0.004	4933.177
3	12,823.747	0.003	12,823.464	0.005	12,823.711	0.003	12,824.145
4	13,002.246	0.062	12,991.382	0.022	12,993.901	0.002	12,994.215
5	23,632.124	0.078	23,621.334	0.032	23,613.557	0.001	23,613.775
6	36,047.788	0.096	36,044.602	0.087	36,013.347	0.000	36,013.226
7	38,444.192	0.001	38,443.250	0.003	38,443.144	0.003	38,444.488
8	49,640.417	0.116	49,653.240	0.142	49,583.475	0.001	49,582.799
9	63,977.974	0.093	63,975.937	0.090	63,920.007	0.002	63,918.563
10	64,006.958	0.049	64,044.242	0.107	63,973.057	0.004	63,975.503
11	78,874.387	0.162	78,944.368	0.251	78,749.088	0.003	78,746.943
12	89,346.670	0.011	89,342.201	0.006	89,332.973	0.004	89,336.686

From the results listed in the tables, we can observe that the original RPIM cannot always provide more accurate solutions than the standard FEM-Q4 in calculating the natural frequency values of this cantilever beam, although the higher order interpolation (not the bilinear interpolation in the FEM-Q4) is employed in the RPIM when the nodal support domain $\alpha_s = 2.5h$. This is mainly caused by the misalignment between the constructed integration cells and the local support domains of the nodal interpolation functions. Owing to this misalignment, the integrands obtained in the original RPIM are not always continuously differentiable, then considerable numerical integration error is generated and leads to an additional loss in computation accuracy. However, from the tables we can observe that very good agreement between the M-RPIM solutions and the reference solutions can be achieved, and the M-RPIM solutions are much more accurate than the RPIM solutions. The main reason for this is that in the M-RPIM a fixed nodal support domain (not a moving support domain), which is built by the centroids of the integration cells, is directly used to perform the required numerical integration; then, the abovementioned misalignment between the integration cells and the local nodal support domains can be easily removed. As a result, the integrands obtained are completely continuously differentiable in the integration cells, so the numerical integration error can be markedly reduced and the computation accuracy can be significantly improved by the present M-RPIM for free vibration analysis. In addition, the vibration modes of the cantilever beam corresponding to the first twelve natural frequency values from the present M-RPIM are plotted in Figure 4; we can observe that the vibration modes obtained are quite stable and the physical mode shapes can be accurately achieved.

4.1.2. Convergence Study

In this subsection, the convergence performance of the numerical solutions from different numerical approaches is investigated in great detail. As shown in Figure 5, the comparison of the relative error (Re) results of the computed natural frequency values from different numerical methods versus the nodal interval ($1/h$) are given; the sign R in the legend of Figure 5 denotes the convergence rate of different numerical techniques. For simplicity, only the first two natural frequency values (Mode 1 and Mode 2) are considered here. From Figure 5, it can be observed that the convergence rate of the original RPIM is unexpectedly lower than the standard FEM-Q4 when the size of the nodal interpolation function support domain is taken as $\alpha_s = 2.5h$. This observation indicates that the misalignment between the integration cells and the local support domain of the nodal shape function in the original RPIM indeed can result in considerable numerical integration error; thus, the convergence rate can be markedly reduced.

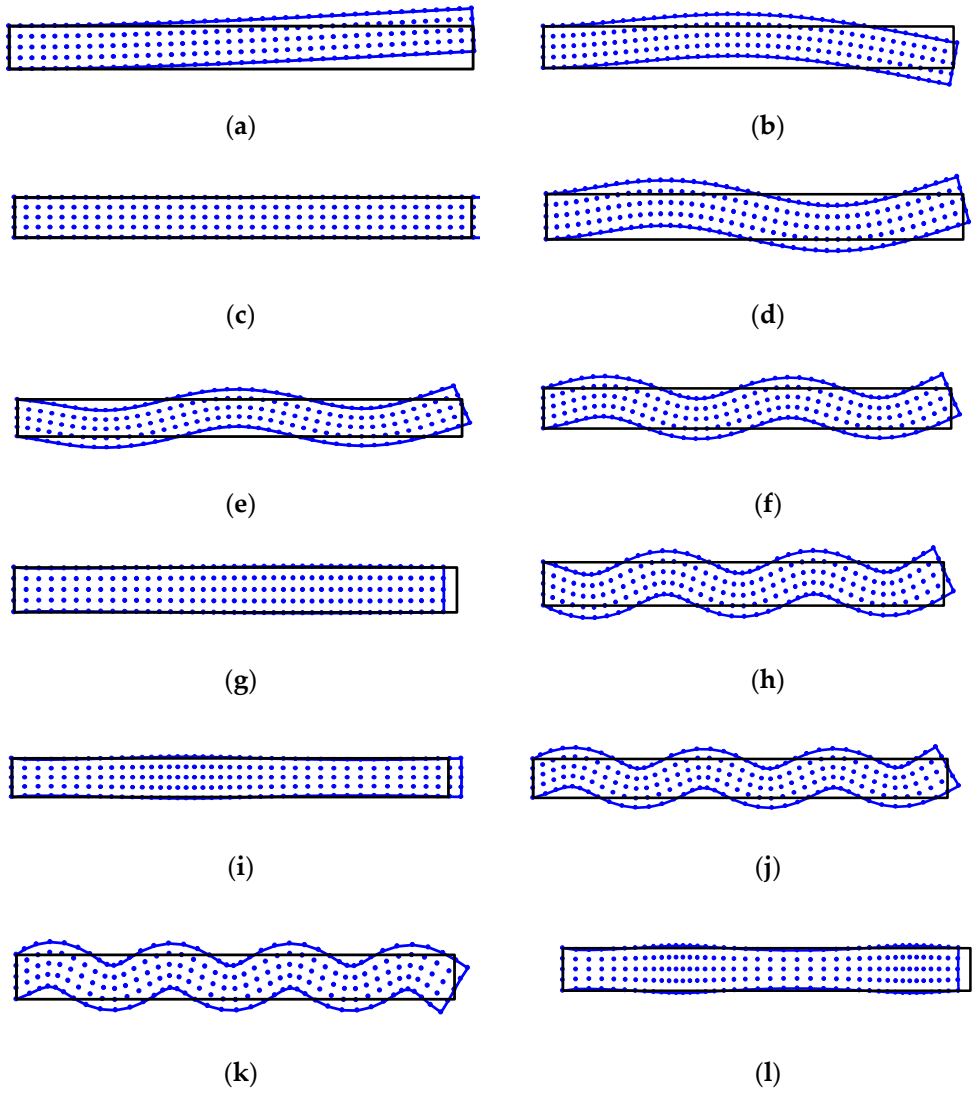

Figure 4. The free vibration modes of cantilever beam corresponding to the first twelve natural frequency values from the present M-RPIM: (**a**) Mode 1; (**b**) Mode 2; (**c**) Mode 3; (**d**) Mode 4; (**e**) Mode 5; (**f**) Mode 6; (**g**) Mode 7; (**h**) Mode 8; (**i**) Mode 9; (**j**) Mode 10; (**k**) Mode 11; (**l**) Mode 12.

However, from Figure 5 we also can see that the present M-RPIM is able to achieve a higher convergence rate than the original RPIM and standard FEM-Q4. These findings again demonstrate that the proposed program in this paper overcomes the misalignment between the constructed integration cells, and that the nodal shape function indeed effectively supports suppression of possible numerical integration error. For free vibration analysis of solids, therefore, the present M-RPIM has a higher convergence rate than the original RPIM and standard FEM-Q4.

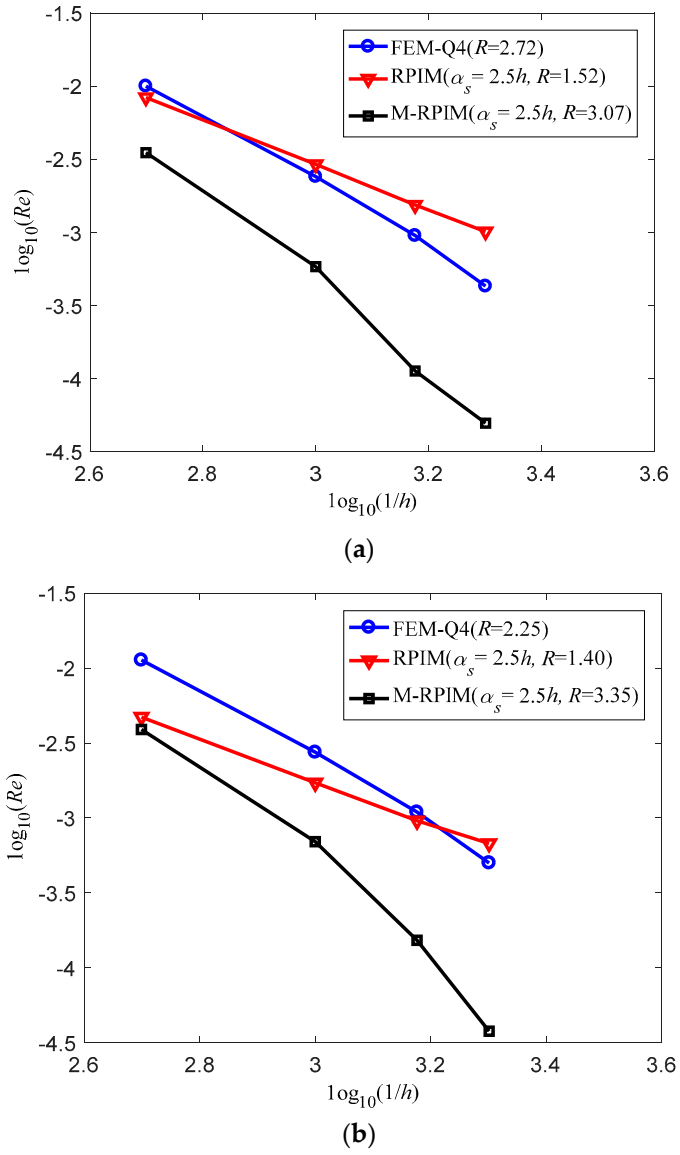

Figure 5. Comparison of the relative error (Re) results of the computed natural frequency values from different numerical methods versus the nodal interval $(1/h)$: (**a**) Mode 1; (**b**) Mode 2.

4.1.3. Computation Efficiency Study

From the analysis and discussion above, it can be observed that the present M-RPIM behaves better than the original RPIM and standard FEM-Q4 in terms of computation accuracy and convergence properties. However, the computation efficiency of the proposed M-RPIM is not yet studied. Note that computation efficiency is also a crucial index to assess the capabilities of numerical methods in engineering computation; comparison of the computation efficiency for the three different numerical methods is performed here. To analyze the computation efficiency, a series of different node arrangement schemes shown in Figure 3 are again employed.

Figure 6 gives the comparison of the relative error results (Re) of the natural frequency values versus the computation cost for the three numerical methods. For simplicity, we still only consider the first two modes. From Figure 6, we can observe that the required computational cost for the standard FEM-Q4 is much less than for the original RPIM and the present M-RPIM when the identical node arrangement scheme is employed. This is because many more quadrature points are used to perform the numerical integration in RPIM and M-RPIM compared to standard FEM-Q4. Nevertheless, the computation accuracy of the

standard FEM-Q4 cannot surpass the M-RPIM because a higher local approximation is used in this meshless numerical technique.

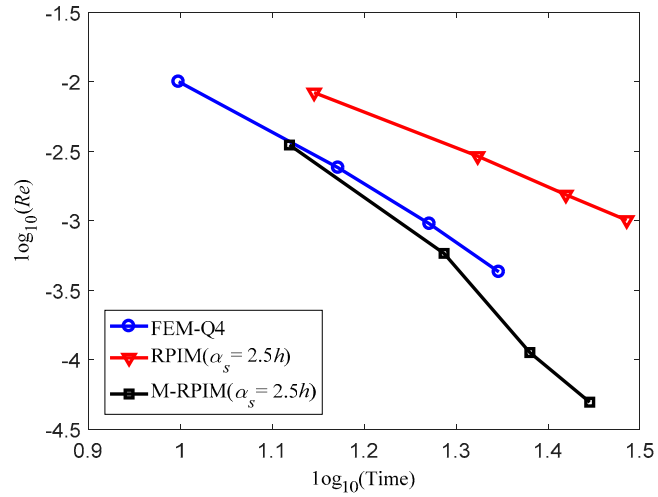

(**a**)

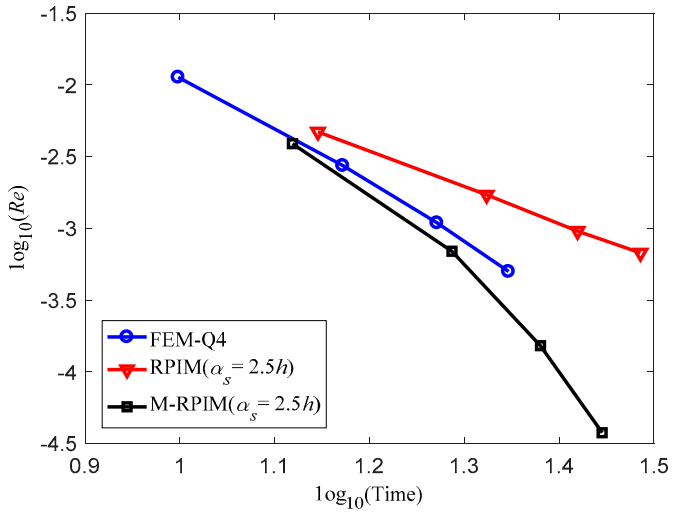

(**b**)

Figure 6. Comparison of the relative error results (Re) of the natural frequency values versus the computation cost for the three different numerical methods: (**a**) Mode 1; (**b**) Mode 2.

From Figure 6, we also can observe that the original RPIM is actually numerically more expensive than the M-RPIM for the identical node arrangement scheme. This is because a moving support domain is used for different quadrature points in the original RPIM. In other words, for each quadrature point, the related operation in determining the support domain (namely the node selection for interpolation) should be performed once, while in the present M-RPIM, a fixed support domain is employed for any quadrature points within one integration cell; hence, the required operation in determining the support domain only should be performed once for each integration cell. Thus, in the M-RPIM, less computational cost is required in the node selection compared to the RPIM. Note that the present M-RPIM also has higher computation accuracy than the original RPIM; hence, the present M-RPIM also possesses higher computation efficiency than the original RPIM in engineering computation. This point can be clearly seen in Figure 6.

4.2. Free Vibration Analysis of the Cantilever Beam with Variable Cross-Section

The second numerical example considered here is a cantilever beam with variable cross-section. The geometric configuration of the variable cross-section beam is shown in Figure 7 and the related material constants are taken as Young's modulus $E = 3 \times 10^7$ Pa, Poisson's ratio $v = 0.3$ and mass density $\rho = 1$ kg/m^3. The regular node arrangement scheme is used to discretize this variable cross-section beam and the corresponding node distributions for the standard FEM-Q4 and the two meshless methods (RPIM and M-RPIM) are given in Figure 8. The first twelve natural frequency values computed using different numerical methods are listed in Table 5. Similar to the first numerical example, the corresponding natural frequency results from the eight-node quadrilateral element (FEM-Q8) with a very refined mesh pattern (5151 nodes and 5000 elements) are also provided as the reference solutions. It is clearly seen that the accuracy of FEM-Q4 results is worse than the original RPIM and the present M-RPIM results. However, the RPIM results are not more accurate than the M-RPIM ones, and the most accurate natural frequency solutions of this variable cross-section cantilever beam can be provided by the present M-RPIM. In addition, the first twelve mode shapes of this variable cross-section cantilever beam obtained from the proposed M-RPIM are depicted in Figure 9. It is easy to find that the eigenmode of this variable cross-section cantilever beam can be accurately predicted by the present M-RPIM. This numerical example demonstrates that the abilities of the original RPIM in engineering computation can be markedly improved by the present M-RPIM.

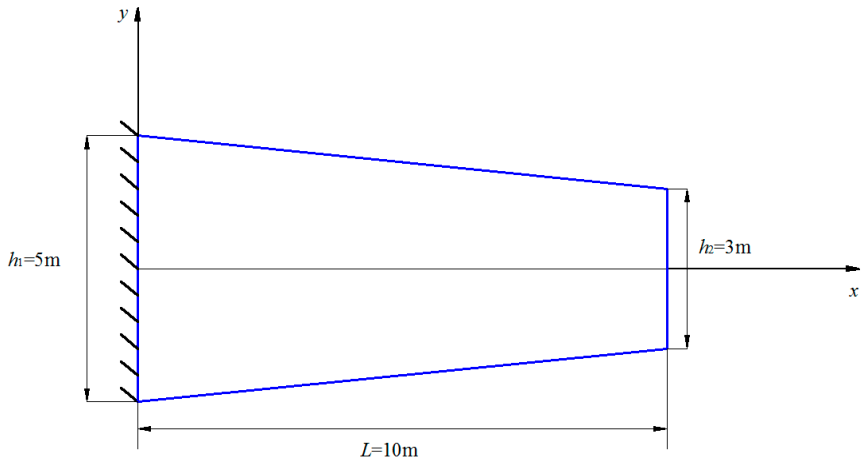

Figure 7. The geometric configuration of the variable cross-section beam in plane stress condition.

Table 5. The first twelve natural frequency values for the variable cross-section cantilever beam computed using different numerical methods.

Mode	FEM-Q4	Error (%)	RPIM	Error (%)	M-RPIM	Error (%)	Ref.
1	41.771	0.333	41.536	0.233	41.678	0.109	41.633
2	147.202	0.781	146.826	0.523	146.335	0.187	146.062
3	151.597	0.058	151.511	0.002	151.532	0.015	151.508
4	298.805	1.349	298.048	1.092	295.483	0.222	294.829
5	412.666	0.326	412.032	0.172	411.396	0.017	411.327
6	442.931	1.685	441.428	1.340	436.366	0.178	435.592
7	528.614	1.053	526.132	0.578	523.667	0.107	523.108
8	601.857	2.143	598.737	1.614	590.187	0.163	589.229
9	619.528	1.005	613.227	0.023	613.441	0.012	613.365
10	671.507	1.529	662.514	0.170	662.167	0.117	661.392
11	710.007	2.389	705.817	1.785	695.000	0.225	693.441
12	713.997	0.802	710.025	0.241	708.647	0.046	708.320

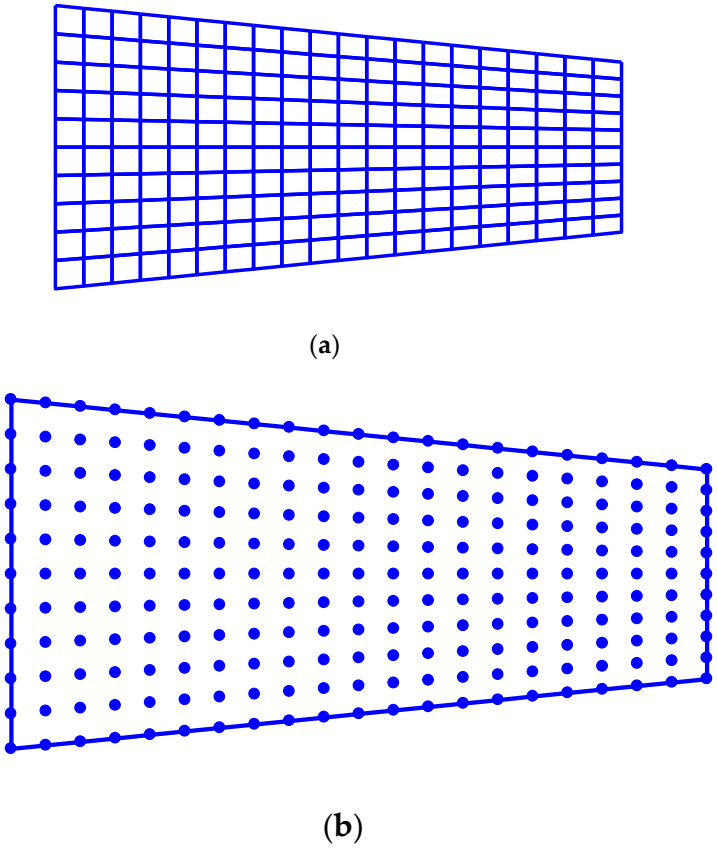

Figure 8. The different node arrangement patterns that are employed to discretize the variable cross-section cantilever beam for different numerical methods: (**a**) mesh pattern used to discretize the variable cross-section cantilever beam for the standard FEM-Q4; (**b**) node arrangement patterns used to discretize the variable cross-section cantilever beam for the RPIM and M-RPIM.

4.3. Free Vibration Analysis of the Cantilever Beam with Holes

The last numerical example is also a cantilever beam in plane stress condition. Unlike the previous numerical examples, the cantilever beam considered here has three identical holes (see Figure 10). The geometric parameters of this beam are given in Figure 10 and the material constants are taken as Young's modulus $E = 2.1 \times 10^{11}$ Pa, Poisson's ratio $v = 0.3$ and mass density $\rho = 8 \times 10^3$ kg/m^3. The node arrangement scheme for the different numerical methods are plotted in Figure 11, and the average nodal interval $h = 0.002$ m. Similar to the previous two numerical examples, the first twelve natural frequency values from the different numerical methods are listed in Table 6, and the corresponding mode shapes from the present M-RPIM are given in Figure 12. In Table 6, the reference solutions are also computed from the eight-node quadrilateral element (FEM-Q8) with a very refined mesh pattern (average node interval $h = 0.0001$ m). Similarly, Table 6 and Figure 12 show that we obtain results similar to those in the previous two numerical examples, namely, the present M-RPIM can generate much more accurate numerical solutions than the original RPIM and FEM-Q4 for free vibration analysis; the present method has great potential for more complicated engineering computation.

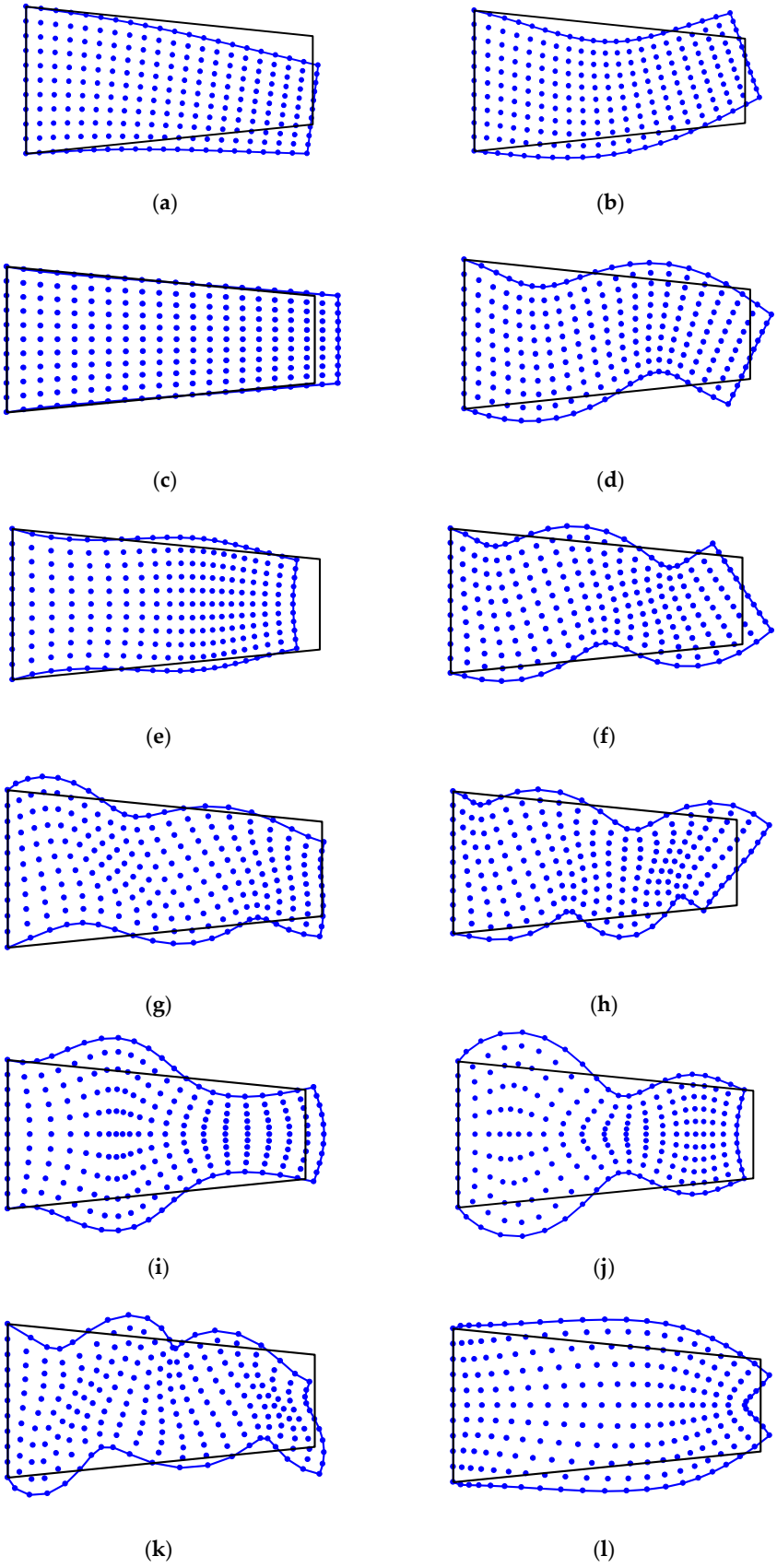

Figure 9. The free vibration modes of the variable cross-section cantilever beam corresponding to the first twelve natural frequency values from the present M-RPIM: (**a**) Mode 1; (**b**) Mode 2; (**c**) Mode 3; (**d**) Mode 4; (**e**) Mode 5; (**f**) Mode 6; (**g**) Mode 7; (**h**) Mode 8; (**i**) Mode 9; (**j**) Mode 10; (**k**) Mode 11; (**l**) Mode 12.

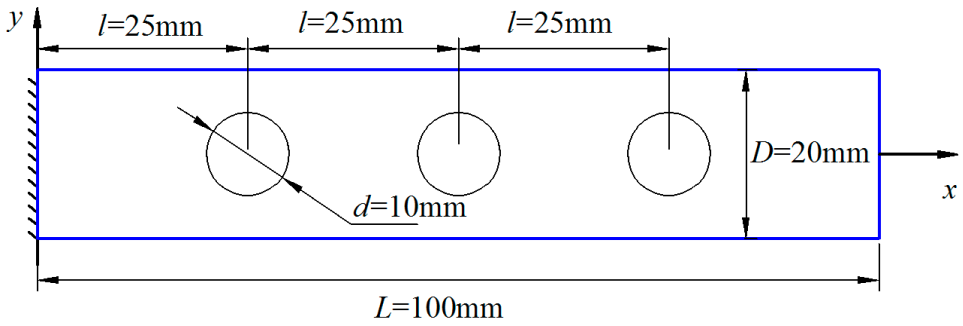

Figure 10. The cantilever beam with three identical holes and in plane stress condition.

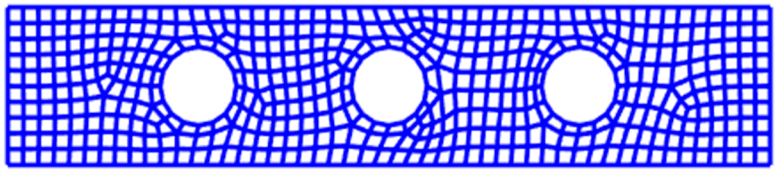

(**a**)

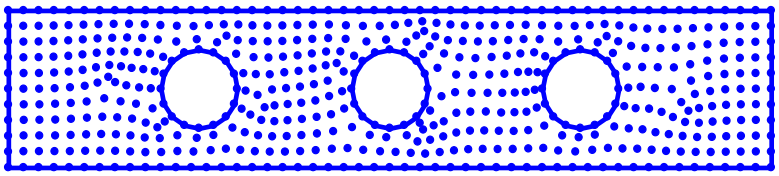

(**b**)

Figure 11. The node arrangement patterns employed to discretize the cantilever beam with three identical holes for the different numerical methods: (**a**) mesh pattern used to discretize the cantilever beam with three identical holes for the standard FEM-Q4; (**b**) node arrangement pattern used to discretize the cantilever beam with three identical holes for the RPIM and M-RPIM.

Table 6. The first twelve natural frequency values computed using different numerical methods for the cantilever beam with three identical holes.

Mode	FEM-Q4	Error (%)	RPIM	Error (%)	M-RPIM	Error (%)	Ref.
1	1626.190	0.617	1612.353	0.239	1618.711	0.154	1616.218
2	8272.300	0.174	8246.759	0.135	8268.312	0.126	8257.923
3	11,373.419	0.791	11,239.656	0.395	11,302.342	0.161	11,284.188
4	19,395.928	1.595	19,004.812	0.454	19,101.194	0.051	19,091.435
5	33,523.877	1.273	33,233.174	0.395	33,231.319	0.390	33,102.326
6	33,972.380	1.786	33,568.275	0.575	33,472.489	0.288	33,376.214
7	37,191.685	2.943	36,443.890	0.873	36,333.778	0.568	36,128.559
8	52,155.832	2.894	51,179.337	0.968	51,042.893	0.699	50,688.744
9	52,582.353	3.420	51,249.812	0.799	51,117.100	0.538	50,843.699
10	55,474.223	2.473	54,470.879	0.620	54,276.585	0.261	54,135.295
11	67,782.825	2.359	66,555.530	0.505	66,471.730	0.379	66,220.863
12	75,775.407	1.343	75,309.818	0.721	74,789.424	0.025	74,771.060

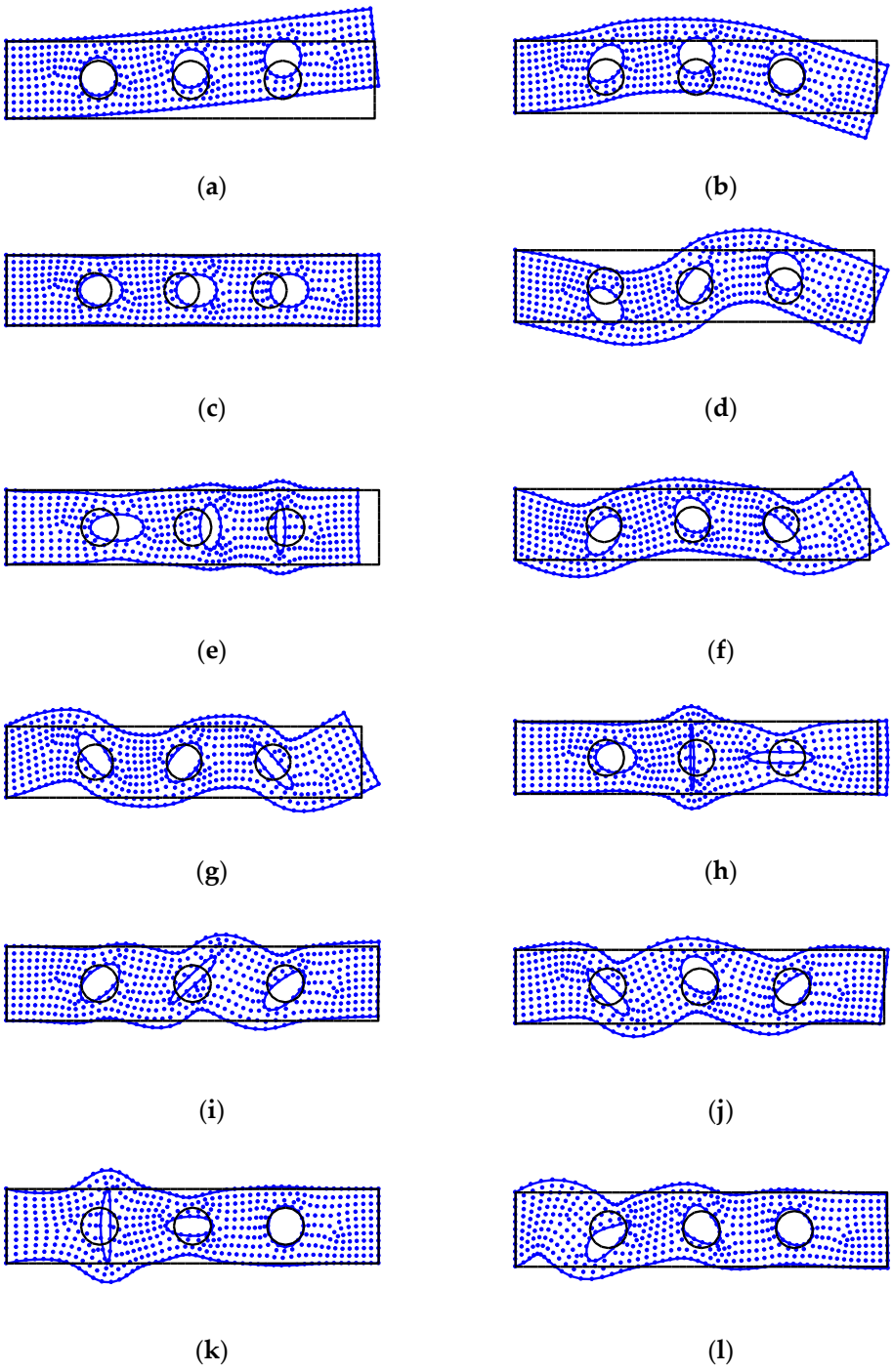

Figure 12. The free vibration modes of the cantilever beam with three identical holes corresponding to the first twelve natural frequency values from the present M-RPIM: (**a**) Mode 1; (**b**) Mode 2; (**c**) Mode 3; (**d**) Mode 4; (**e**) Mode 5; (**f**) Mode 6; (**g**) Mode 7; (**h**) Mode 8; (**i**) Mode 9; (**j**) Mode 10; (**k**) Mode 11; (**l**) Mode 12.

5. Conclusions

In this work, a modified radial point interpolation method (M-RPIM) is proposed to enhance the capacities of the original RPIM for the free vibration analysis of two-dimensional solids. In the present M-RPIM, the numerical approximation established in integration cells is continuously differentiable while the corresponding numerical approximation in the original RPIM is always not continuously differentiable. Therefore, the possible numerical integration error in the original RPIM can be markedly reduced by the present M-RPIM.

Several supporting numerical examples are employed to investigate fully and in detail the performance of the proposed M-RPIM in solving free vibration problems. It is demonstrated that the proposed M-RPIM not only is able to surpass the original RPIM and the standard FEM-Q4 in terms of computation accuracy and convergence properties when the identical node arrangement scheme is employed, but the proposed method also has higher computation efficiency. This is because the fixed support domain is employed for any quadrature points in the integration cells; hence, the additional operations to determine the support domain for each quadrature point are not required. Owing to these excellent features, the present M-RPIM has great potential for solving more complex problems in practical engineering application.

Author Contributions: Conceptualization, T.S. and Y.C.; methodology, Y.C.; software, P.W.; validation, T.S. and Y.C.; formal analysis, T.S.; investigation, T.S.; resources, Y.C.; data curation, T.S.; writing—original draft preparation, T.S.; writing—review and editing, T.S.; visualization, T.S.; supervision, Y.C.; funding acquisition, G.Z. All authors have read and agreed to the published version of the manuscript.

Funding: This research was funded by the State Key Laboratory of Ocean Engineering (Shanghai Jiao Tong University) (Grant No. GKZD010081); the National Natural Science Foundation of China (Grant No. 51909201); the Open Fund of Key Laboratory of High Performance Ship Technology (Wuhan University of Technology), Ministry of Education (Grant No. gxnc21112701 and No. gxnc18041401); and the National Key Laboratory on Ship Vibration and Noise (Grant No. 6142204210208).

Institutional Review Board Statement: Not applicable.

Informed Consent Statement: Not applicable.

Data Availability Statement: The data used to support the findings of this study are available from the corresponding author upon request.

Acknowledgments: We thank Qiang Gui for the helpful suggestions to revise the present paper.

Conflicts of Interest: The authors declare no conflict of interest.

References

1. Bathe, K.J. *Finite Element Procedures*, 2nd ed.; Prentice Hall: Watertown, MA, USA, 2014.
2. Li, J.P.; Fu, Z.J.; Gu, Y.; Qin, Q.H. Recent advances and emerging applications of the singular boundary method for large-scale and high-frequency computational acoustics. *Adv. Appl. Math. Mech.* **2022**, *14*, 315–343. [CrossRef]
3. Wu, F.; Zhou, G.; Gu, Q.Y.; Chai, Y.B. An enriched finite element method with interpolation cover functions for acoustic analysis in high frequencies. *Eng. Anal. Bound. Elem.* **2021**, *129*, 67–81. [CrossRef]
4. Gu, Y.; Fan, C.M.; Fu, Z.J. Localized method of fundamental solutions for three-dimensional elasticity problems: Theory. *Adv. Appl. Math. Mech.* **2021**, *13*, 1520–1534.
5. Liu, C.S.; Qiu, L.; Lin, J. Simulating thin plate bending problems by a family of two-parameter homogenization functions. *Appl. Math. Model.* **2020**, *79*, 284–299. [CrossRef]
6. Li, J.P.; Zhang, L.; Qin, Q.H. A regularized method of moments for three-dimensional time-harmonic electromagnetic scattering. *Appl. Math. Lett.* **2021**, *112*, 106746. [CrossRef]
7. Qiu, L.; Lin, J.; Wang, F.J.; Qin, Q.H.; Liu, C.S. A homogenization function method for inverse heat source problems in 3D functionally graded materials. *Appl. Math. Model.* **2021**, *91*, 923–933. [CrossRef]
8. Gu, Y.; Lei, J. Fracture mechanics analysis of two-dimensional cracked thin structures (from micro- to nano-scales) by an efficient boundary element analysis. *Results Math.* **2021**, *11*, 100172. [CrossRef]
9. Li, J.P.; Gu, Y.; Qin, Q.H.; Zhang, L. The rapid assessment for three-dimensional potential model of large-scale particle system by a modified multilevel fast multipole algorithm. *Comput. Math. Appl.* **2021**, *89*, 127–138. [CrossRef]
10. Chai, Y.B.; Bathe, K.J. Transient wave propagation in inhomogeneous media with enriched overlapping triangular elements. *Comput. Struct.* **2020**, *237*, 106273. [CrossRef]
11. Chai, Y.B.; Li, W.; Liu, Z.Y. Analysis of transient wave propagation dynamics using the enriched finite element method with interpolation cover functions. *Appl. Math. Comput.* **2022**, *412*, 126564. [CrossRef]
12. Li, Y.C.; Dang, S.N.; Li, W.; Chai, Y.B. Free and Forced Vibration Analysis of Two-Dimensional Linear Elastic Solids Using the Finite Element Methods Enriched by Interpolation Cover Functions. *Mathematics* **2022**, *10*, 456. [CrossRef]
13. Liu, M.Y.; Gao, G.J.; Zhu, H.F.; Jiang, C. A cell-based smoothed finite element method stabilized by implicit SUPG/SPGP/Fractional step method for incompressible flow. *Eng. Anal. Bound. Elem.* **2021**, *124*, 194–210. [CrossRef]

14. Chai, Y.B.; Gong, Z.X.; Li, W.; Li, T.Y.; Zhang, Q.F.; Zou, Z.H.; Sun, Y.B. Application of smoothed finite element method to two dimensional exterior problems of acoustic radiation. *Int. J. Comput. Methods* **2018**, *15*, 1850029. [CrossRef]
15. Liu, M.Y.; Gao, G.J.; Zhu, H.F.; Jiang, C.; Liu, G.R. A cell-based smoothed finite element method (CS-FEM) for three-dimensional incompressible laminar flows using mixed wedge-hexahedral element. *Eng. Anal. Bound. Elem.* **2021**, *133*, 269–285. [CrossRef]
16. Wang, T.T.; Zhou, G.; Jiang, C.; Shi, F.C.; Tian, X.D.; Gao, G.J. A coupled cell-based smoothed finite element method and discrete phase model for incompressible laminar flow with dilute solid particles. *Eng. Anal. Bound. Elem.* **2022**, *143*, 190–206. [CrossRef]
17. Li, W.; Gong, Z.X.; Chai, Y.B.; Cheng, C.; Li, T.Y.; Zhang, Q.F.; Wang, M.S. Hybrid gradient smoothing technique with discrete shear gap method for shell structures. *Comput. Math. Appl.* **2017**, *74*, 1826–1855. [CrossRef]
18. Liu, G.R. *Mesh Free Methods: Moving Beyond the Finite Element Method*; CRC Press: Boca Raton, FL, USA, 2009.
19. Cheng, S.F.; Wang, F.J.; Wu, G.Z.; Zhang, C.X. semi-analytical and boundary-type meshless method with adjoint variable formulation for acoustic design sensitivity analysis. *Appl. Math. Lett.* **2022**, *131*, 108068. [CrossRef]
20. Lin, J. Simulation of 2D and 3D inverse source problems of nonlinear time-fractional wave equation by the meshless homogenization function method. *Eng. Comput.* **2021**. [CrossRef]
21. Lin, J.; Bai, J.; Reutskiy, S.; Lu, J. A novel RBF-based meshless method for solving time-fractional transport equations in 2D and 3D arbitrary domains. *Eng. Comput.* **2022**. [CrossRef]
22. Lin, J.; Zhang, Y.H.; Reutskiy, S.; Feng, W. A novel meshless space-time backward substitution method and its application to nonhomogeneous advection-diffusion problems. *Appl. Math. Comput.* **2021**, *398*, 125964. [CrossRef]
23. Wang, C.; Wang, F.J.; Gong, Y.P. Analysis of 2D heat conduction in nonlinear functionally graded materials using a local semi-analytical meshless method. *AIMS Math.* **2021**, *6*, 12599–12618. [CrossRef]
24. Gu, Y.; Sun, H.G. A meshless method for solving three-dimensional time fractional diffusion equation with variable-order derivatives. *Appl. Math. Model.* **2020**, *78*, 539–549. [CrossRef]
25. Li, X.; Li, S. A fast element-free Galerkin method for the fractional diffusion-wave equation. *App. Math. Lett.* **2021**, *122*, 107529. [CrossRef]
26. Li, X.; Li, S. A linearized element-free Galerkin method for the complex Ginzburg–Landau equation. *Comput. Math. Appl.* **2021**, *90*, 135–147. [CrossRef]
27. Atluri, S.N.; Kim, H.G.; Cho, J.Y. Critical assessment of the truly meshless local PetrovGalerkin (MLPG), and local boundary integral equation (LBIE) methods. *Comput. Mech.* **1999**, *24*, 348–372. [CrossRef]
28. Liu, W.K.; Jun, S.; Zhang, Y.F. Reproducing kernel particle methods. *Int. J. Numer. Methods Fluids* **1995**, *20*, 1081–1106. [CrossRef]
29. Qu, J.; Dang, S.N.; Li, Y.C.; Chai, Y.B. Analysis of the interior acoustic wave propagation problems using the modified radial point interpolation method (M-RPIM). *Eng. Anal. Bound. Elem.* **2022**, *138*, 339–368. [CrossRef]
30. Gui, Q.; Zhang, Y.; Chai, Y.B.; You, X.Y.; Li, W. Dispersion error reduction for interior acoustic problems using the radial point interpolation meshless method with plane wave enrichment functions. *Eng. Anal. Bound. Elem.* **2022**, *143*, 428–441. [CrossRef]
31. Qu, W.Z.; He, H. A GFDM with supplementary nodes for thin elastic plate bending analysis under dynamic loading. *Appl. Math. Lett.* **2022**, *124*, 107664. [CrossRef]
32. Qu, W.Z.; Gao, H.W.; Gu, Y. Integrating Krylov deferred correction and generalized finite difference methods for dynamic simulations of wave propagation phenomena in long-time intervals. *Adv. Appl. Math. Mech.* **2021**, *13*, 1398–1417.
33. Xi, Q.; Fu, Z.J.; Li, Y.; Huang, H. A hybrid GFDM–SBM solver for acoustic radiation and propagation of thin plate structure under shallow sea environment. *J. Theor. Comput. Acous.* **2020**, *28*, 2050008. [CrossRef]
34. Fu, Z.J.; Xie, Z.Y.; Ji, S.Y.; Tsai, C.C.; Li, A.L. Meshless generalized finite difference method for water wave interactions with multiple-bottom-seated-cylinder-array structures. *Ocean Eng.* **2020**, *195*, 106736. [CrossRef]
35. Zheng, Z.Y.; Li, X.L. Theoretical analysis of the generalized finite difference method. *Comput. Math. Appl.* **2022**, *120*, 1–14. [CrossRef]
36. Wang, F.; Fan, C.M.; Zhang, C.; Lin, J. A localized space-time method of fundamental solutions for diffusion and convection-diffusion problems. *Adv. Appl. Math. Mech.* **2020**, *12*, 940–958. [CrossRef]
37. Fu, Z.J.; Xi, Q.; Li, Y.; Huang, H.; Rabczuk, T. Hybrid FEM–SBM solver for structural vibration induced underwater acoustic radiation in shallow marine environment. *Comput. Methods Appl. Mech. Eng.* **2020**, *369*, 113236. [CrossRef]
38. Fu, Z.J.; Chen, W.; Wen, P.H.; Zhang, C.Z. Singular boundary method for wave propagation analysis in periodic structures. *J. Sound Vib.* **2018**, *425*, 170–188. [CrossRef]
39. Li, J.P.; Zhang, L. High-precision calculation of electromagnetic scattering by the Burton-Miller type regularized method of moments. *Eng. Anal. Bound. Elem.* **2021**, *133*, 177–184. [CrossRef]
40. Li, J.P.; Zhang, L.; Qin, Q.H. A regularized fast multipole method of moments for rapid calculation of three-dimensional time-harmonic electromagnetic scattering from complex targets. *Eng. Anal. Bound. Elem.* **2022**, *142*, 28–38. [CrossRef]
41. Zhang, Y.O.; Dang, S.N.; Li, W.; Chai, Y.B. Performance of the radial point interpolation method (RPIM) with implicit time integration scheme for transient wave propagation dynamics. *Comput. Math. Appl.* **2022**, *114*, 95–111. [CrossRef]
42. You, X.Y.; Li, W.; Chai, Y.B. A truly meshfree method for solving acoustic problems using local weak form and radial basis functions. *Appl. Math. Comput.* **2020**, *365*, 124694. [CrossRef]
43. Chai, Y.B.; You, X.Y.; Li, W. Dispersion Reduction for the Wave Propagation Problems Using a Coupled "FE-Meshfree" Triangular Element. *Int. J. Comput. Methods* **2020**, *17*, 1950071. [CrossRef]

44. Li, W.; Zhang, Q.; Gui, Q.; Chai, Y.B. A coupled FE-Meshfree triangular element for acoustic radiation problems. *Int. J. Comput. Methods* **2021**, *18*, 2041002. [CrossRef]
45. Wang, F.; Zhao, Q.; Chen, Z.; Fan, C.M. Localized Chebyshev collocation method for solving elliptic partial differential equations in arbitrary 2D domains. *Appl. Math. Comput.* **2021**, *397*, 125903. [CrossRef]
46. Xi, Q.; Fu, Z.J.; Zhang, C.Z.; Yin, D.S. An efficient localized Trefftz-based collocation scheme for heat conduction analysis in two kinds of heterogeneous materials under temperature loading. *Comput. Struct.* **2021**, *255*, 106619. [CrossRef]
47. Xi, Q.; Fu, Z.J.; Wu, W.J.; Wang, H.; Wang, Y. A novel localized collocation solver based on Trefftz basis for Potential-based Inverse Electromyography. *Appl. Math. Comput.* **2021**, *390*, 125604. [CrossRef]
48. Li, X.; Li, S. A finite point method for the fractional cable equation using meshless smoothed gradients. *Eng. Anal. Bound. Elem.* **2022**, *134*, 453–465. [CrossRef]
49. Fu, Z.J.; Yang, L.W.; Xi, Q.; Liu, C.S. A boundary collocation method for anomalous heat conduction analysis in functionally graded materials. *Comput. Math. Appl.* **2021**, *88*, 91–109. [CrossRef]
50. Tang, Z.; Fu, Z.J.; Sun, H.; Liu, X. An efficient localized collocation solver for anomalous diffusion on surfaces. *Fract. Calc. Appl. Anal.* **2021**, *24*, 865–894. [CrossRef]
51. Xi, Q.; Fu, Z.J.; Rabczuk, T.; Yin, D. A localized collocation scheme with fundamental solutions for long-time anomalous heat conduction analysis in functionally graded materials. *Int. J. Heat Mass Tran.* **2021**, *180*, 121778. [CrossRef]
52. Dolbow, J.; Belytschko, T. Numerical integration of the Galerkin weak form in meshfree methods. *Comput. Mech.* **1999**, *23*, 219–230. [CrossRef]
53. Liu, G.R.; Gu, Y.T. Assessment and applications of point interpolation methods for computational mechanics. *Int. J. Numer. Meth. Engng.* **2004**, *59*, 1373–1397. [CrossRef]